Chapter 6

MnBi/Co@C nanocomposites

Chapter 6: MnBi/Co@C nanocomposites

6.1 Introduction

From the previous chapters, it has been observed that cryogenic ball milled MnBi sample displayed superior magnetic properties than room-temperature milled one. In addition, as seen in the case of nanocomposites (discussed in chapters 4 and 5), the addition of soft magnetic phases up to certain proportions increases the overall $(BH)_{max}$ by improving the M_S and M_r values. However, the optimum results were obtained with 10 % addition of Fe_3C@C and 15% addition of FeNi@C with MnBi. Further additions of these soft phases led to deterioration of the coercivity value and consequently the energy products. Therefore, Co@C with considerable anisotropy field, which would not reduce the coercivity, was selected as another soft phase.

Since Co@C can not only contribute with appreciable magnetization values but also have large magnetocrystalline anisotropy. Owing to the high M_S and H_c values, in combination with appropriate particle size, the effect of Co@C addition on the hard phase should provide better $(BH)_{max}$ values. The micromagnetic finite element studies on MnBi/Co system also predicted that the soft phase with higher anisotropy field is preferred [1]. Such cases the amount of soft phase in the nanocomposite can be increased which would improve M_S and M_r values without deteriorating the H_C value. It was further predicted that an energy product up to 50 MGOe can be achieved for the perfect exchange coupled magnets of Co and LTP MnBi [2]. Thus, MnBi/Co@C nanocomposites were prepared using cryogenic ball milling and their magnetic properties were evaluated.

6.2. Results and discussion

Figure 6.1a refers to the x-ray diffraction pattern obtained from the Co@C nanoparticles. The obtained peaks were indexed with the help of JCPDF Files: JCPDS 05-0727 and JCPDS 15-0806, corresponding to the fcc structured Co and hcp Co respectively. The indexing of the diffraction pattern suggests that a mixture of fcc and hcp phases has formed. According to Dinega et al., such an existence of both the phases is most probable if the synthesis methodology employs higher temperature steps [3]. This is due to the low activation barrier associated with the formation of stacking faults at elevated temperatures. Peak splitting at 2θ of 76º, overlapping peak for fcc and hcp, is a signature for the phase mixture.

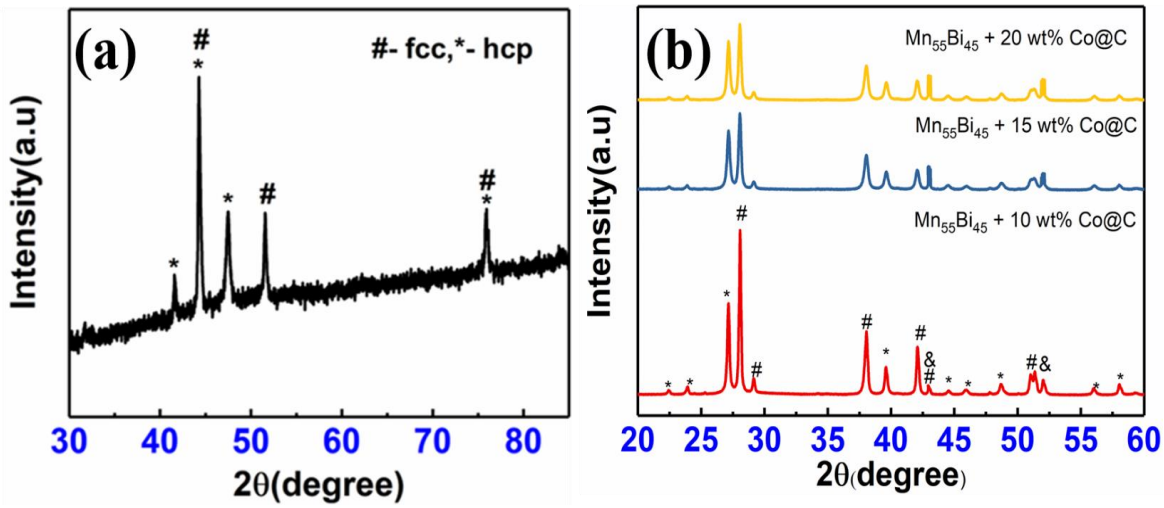

Figure 6.1. X-ray diffraction patterns of (a) Co@C nanoparticles and (b) $Mn_{55}Bi_{45}$ with 10, 15, and 20 wt. % of Co@C after 2 h of cryo-milling. (*-Bi phase, #- LTP MnBi phase, &-Co@C) ((hkl) indexing is similar to Figure 3.1 and not marked for better comprehensibility).

In addition, the peak at 42º, corresponding to the (200) atomic plane of fcc Co, displayed a slight shift in peak position and peak broadening, in comparison to the pure fcc phase. This is also in agreement with the prior reports, which attribute to the presence of hcp stacking faults in the nanoparticles to the observed features [4,5].

The relative percentages of fcc and hcp phases was found to be 37 % and 63 % respectively, as per the calculations made using X-pert Highscore software. The baseline rise, a feature of carbon containing materials also is an indication of the presence of carbon. Apart from this feature and in concurrence with the earlier reports, there is no direct evidence of carbon peaks in the material, within the detection limits of the instrument [6]. The average crystallite size of the Co@C nanoparticles was calculated from the Scherrer's formula [7]. The calculation was done individually for fcc peak at 52º peak whereas with 42 and 48º peaks for hcp phase. These calculations showed that the average crystallite sizes for hcp phase in Co@C was about ~ 32 nm, while that of fcc phase was found to be ~ 27 nm.

Figure 6.1b, reveals the XRD patterns of the $Mn_{55}Bi_{45}$/Co@C (10, 15 and 20 wt.%) nanocomposites. They show the presence of three different phases like other nanocomposites (chapters 4 and 5). Along with the desired LTP phase, Bi and minor amounts of Mn can be seen in the figure 6.1 b. In addition, the peak at 42º corresponding to Co, can be seen to increase gradually, along with the increasing content of Co@C. The average crystallite size of the nanocomposites was calculated using the Williamson-Hall plot and found to be 122, 107 and 103 nm for 10, 15 and 20 wt.% of Co@C respectively. The lattice strain values variation can be seen the below Figure 6.2.

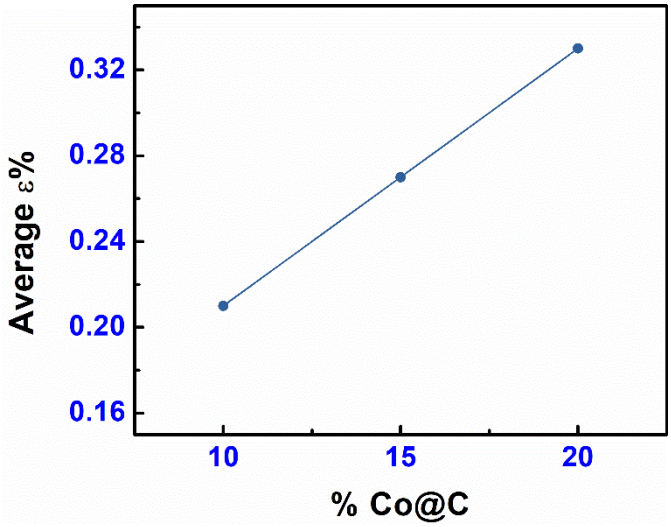

Figure 6.2. The variation in lattice strain of cryo-milled samples with increased percentage of Co@C soft phase.

SEM analysis:

Figure 6. depicts the SEM analysis of Co@C nanoparticles. The SE micrographs, as seen in Figure 6.3a, reveals that the particles are fused to each other. This is because the sample was synthesized at 700 ºC where it would increase the chance of collision fusion among Co metal particles, including the reactivity of Co and C atoms, which resulted in the increase of particle size [8].

Therefore, the rise of calcination temperature promoted the formation and growth of Co@C nanoparticles. The surfaces of the Co@C nanoparticles are clean and smooth, and no other type of carbon nanostructures could be observed, implying high purity of the Co@C nanoparticles. The EDS spectrum (Figure 6.3b) confirmed the presence of Co and C. The corresponding EDS mapping showed the uniform distribution of Co and C.

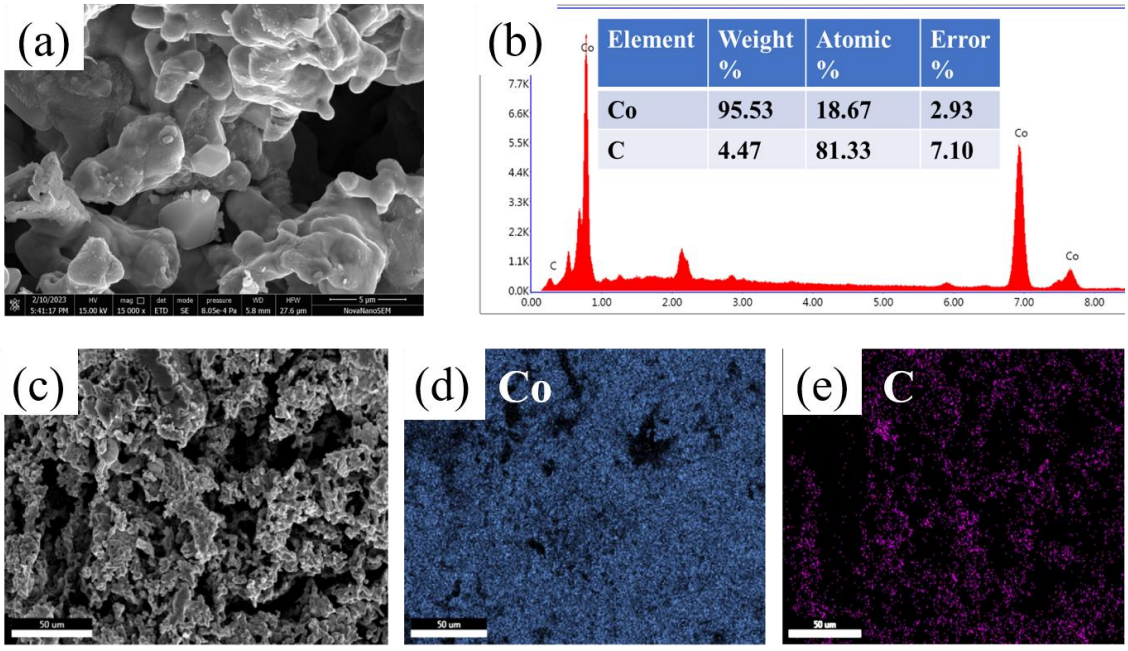

Figure 6.3. (a) SEM micrograph of Co@C in SE mode, (b) EDS spectrum showing the quantitative composition of Co@C, (c) Low magnification SE image and its corresponding elemental mapping of (d) Co and (e) C.

Further figure 6.4a shows the SE micrograph of the randomly shaped nanoparticles of MnBi/Co@C (15 wt.%) composite after 2 h of cryogenic ball milling.

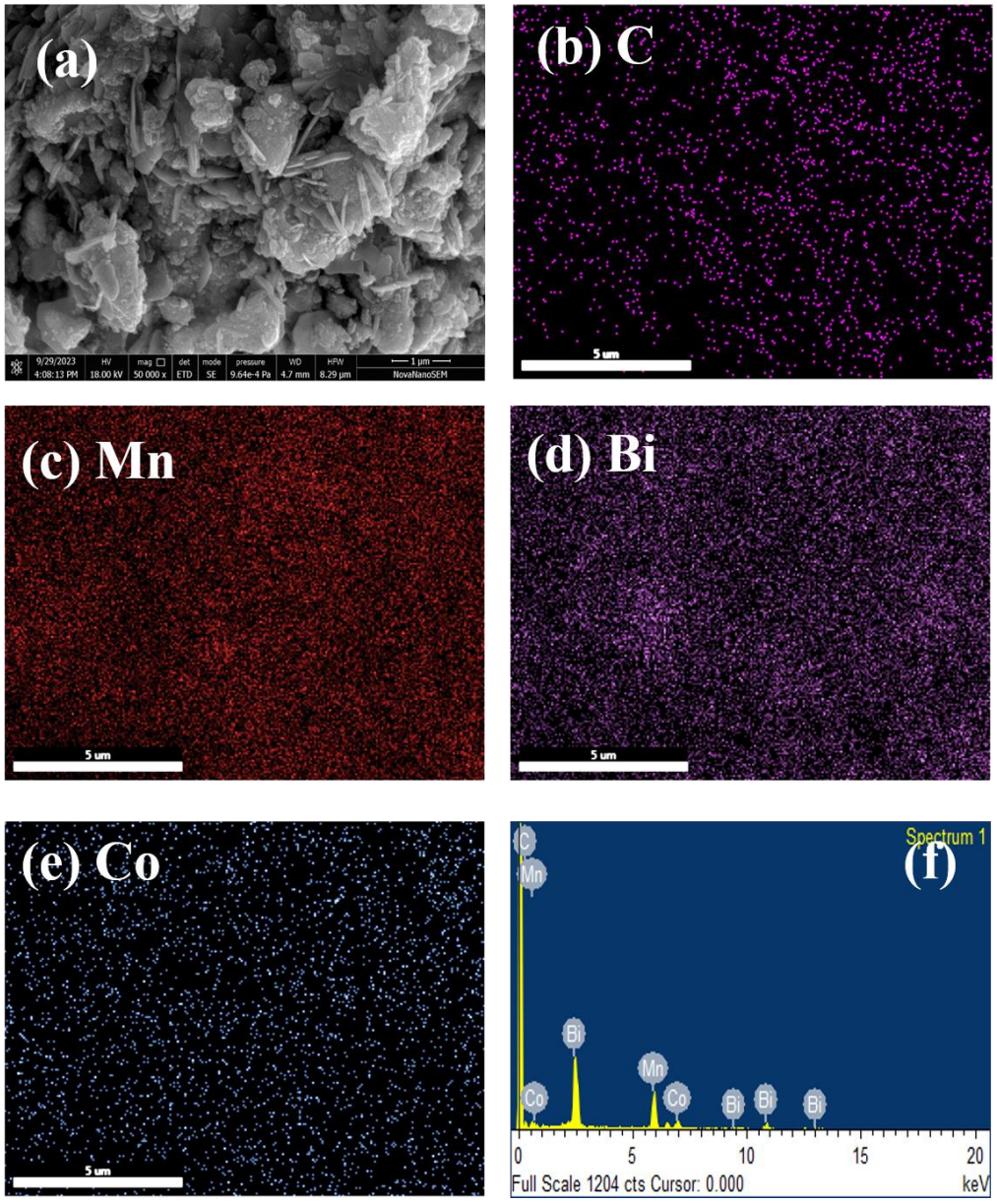

Figure 6.4. (a) Scanning electron micrograph of cryo-milled MnBi/Co@C (15 wt.%) nanocomposite, its (b-e) elemental mapping of all the constituents and (f) the corresponding EDS spectrum.

The composition of elements is corroborated by the EDS spectrum which shows the corresponding peaks of individual elements (Fig 6.4f). The spectrum shows peaks corresponding to the elements Mn, Bi, Co and C. The elemental mapping of the nanocomposite is also shown in Fig 6.4 (b-e) which displays a homogenous distribution of all the constituents.

TEM analysis:

The TEM analysis of the Co@C nanoparticles is presented in Figure 6.5. The Figure 6.5a, shows the bright field image of the nanoparticles, which consist of outer graphitic layers and inner Co nanoparticles, which is consistent with earlier reported literature [9,10]. According to the particle size distribution (inset of Fig.6. 4a) obtained from the Image J analysis of BF image, the average size of the Co nanoparticles in the Co@C composite structure is about 5.5 nm with the size distribution range of 2.6-20.3 nm.

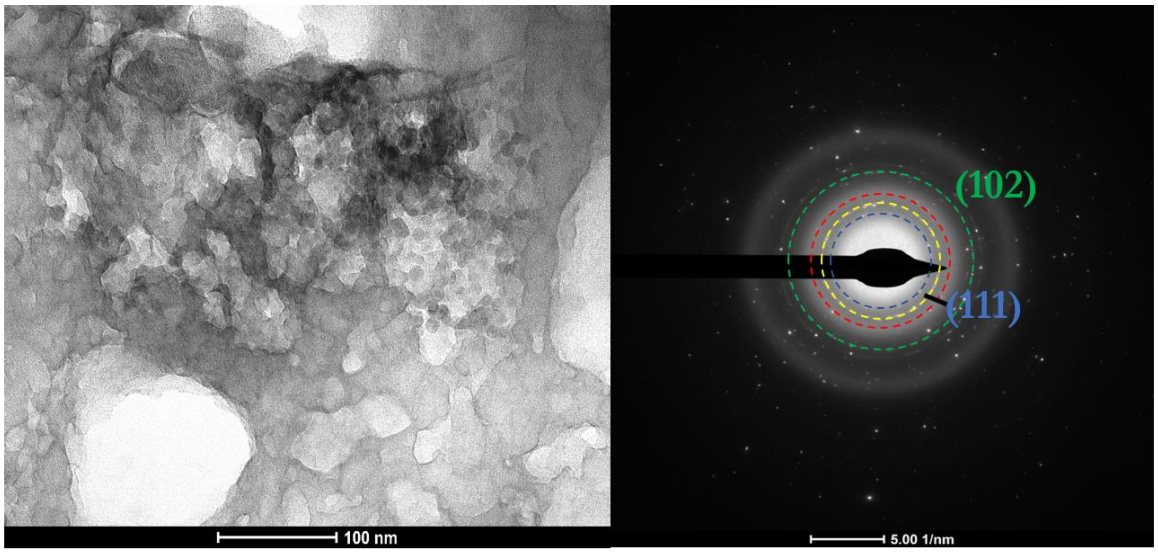

Figure 6.5. (a) Bright-field image and (b) corresponding diffraction pattern of Co@C nanoparticles.

The carbon-encapsulated layers are clear and integrated, with a thickness of 5–10 nm, which can provide effective protection from oxidation to the Co nanoparticles and keep their physical and chemical stability. The diffraction patterns (Fig. 6.5b) also confirm the good crystal structure of Co nanoparticles and can be ascribed to the (111) plane of fcc Co and (102) plane of hcp Co.

The TEM micrograph of nanocomposite obtained after 2 h of cryomilling of 15 wt.%Co@C with $Mn_{55}Bi_{45}$ is shown in Figure 6.6.

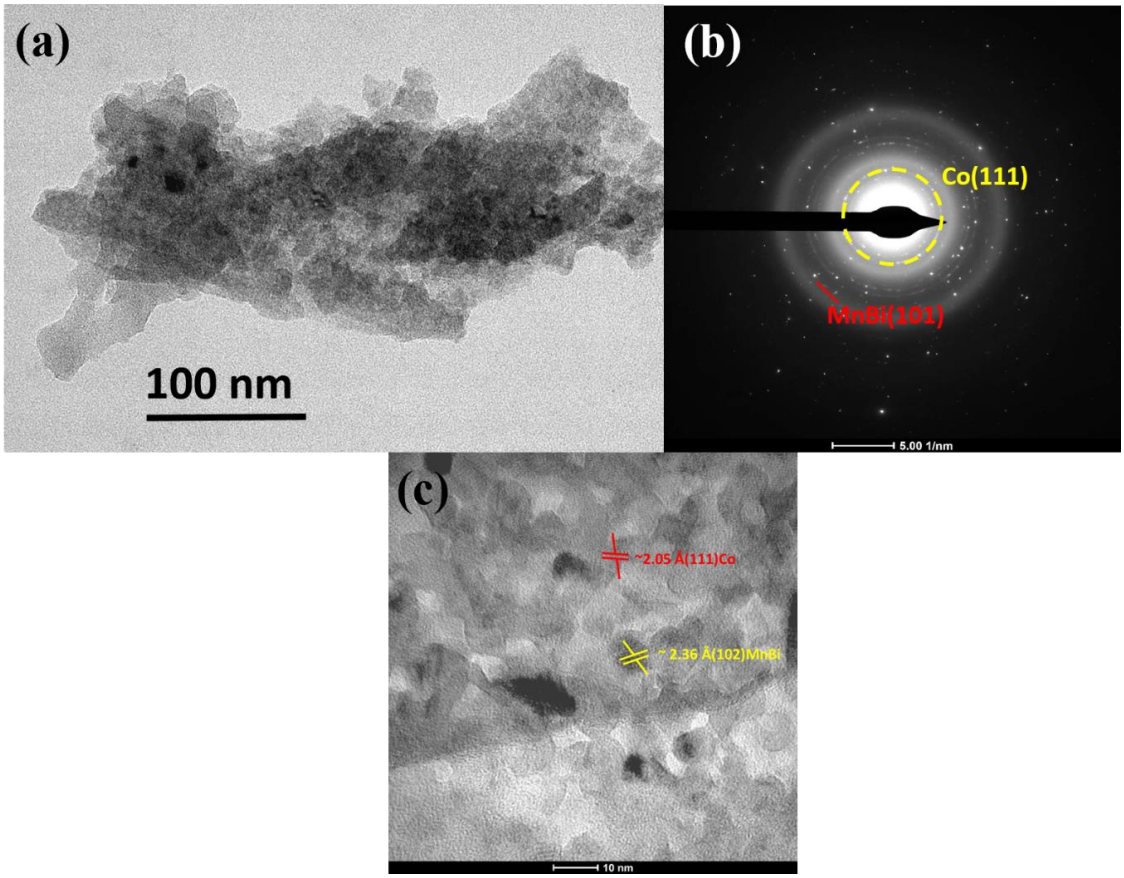

Figure 6.6. Transmission electron micrograph (a) Bright field image (b) corresponding diffraction pattern, (c) high resolution image with d-spacing fringes of nanocomposites of $Mn_{55}Bi_{45}$/Co@C (15 wt.%).

The figure 6.6a corresponds to the bright field micrograph showing a contrast in colour arising from the different phases of the nanocomposite. The corresponding SAD pattern (Figure 6.6b) corroborates the presence of both, soft magnetic (Co@C) and hard magnetic (LTP MnBi) phases in the material. The interplanar spacing has been calculated using the HR images of the nanocomposite as seen in Figure 6.6c. The high-resolution image, reveals the different phases present in the composite and their interplanar spacing have matched with that of LTP MnBi and Co phases.

Raman spectroscopy analysis:

Figure 6.7 shows the Raman spectrum of Co@C nanoparticles. It exhibit two Raman bands at ~1345 cm^{-1} (D band) and ~1600 cm^{-1} (G band), which are associated with the vibrations of carbon atoms with dangling bonds for the in-plane terminations of disordered graphite (D) and the vibrations in all sp^2-bonded carbon atoms in a 2D hexagonal lattice (G), respectively [11,12]. The relative intensity values (I_D/I_G) for the Co@C was around 0.90. The use of 700 °C calcination temperature has resulted in an obvious improvement in the degree of graphitization. Metal-metal and metal-ligand vibrations have frequencies below 750 cm^{-1} [13]. This mode is the most sensitive to reveal the strength of metal-metal bonding. The symmetric and asymmetric stretching frequencies of metal lie in a range of 150-650 cm^{-1} depending on the metal-metal bonding and the symmetric stretching mode strongly active in Raman spectra. Moreover, the metal-related line intensity is enhanced in resonance Raman spectra because it excites the molecules in the red-end of their d-d transition. The Raman peaks below 750 cm^{-1} are attributed to the Co-Co stretching mode [14,15], observed in Figure 6.7.

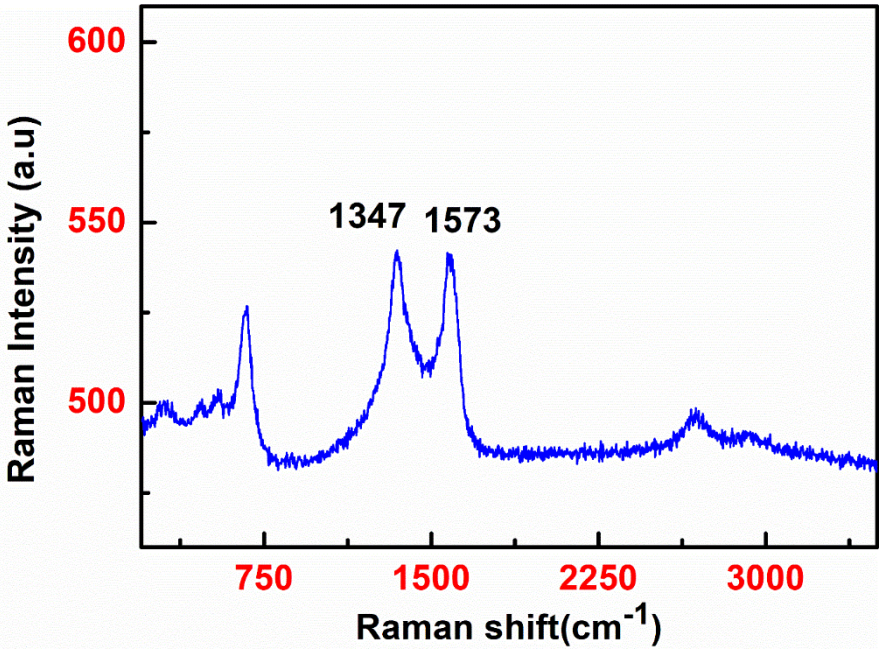

Figure 6.7. Raman spectra of Co@C nanoparticles.

Magnetic analysis:

The room-temperature magnetic properties of Co@C nanoparticles was evaluated under an applied field of ±30 kOe as shown in Figure 6.8. The M vs. H curve showed a soft ferromagnetic behavior, with a saturation magnetization value of ~ 140 emu/g, remanent magnetization of ~ 34 emu/g and a coercivity value of 470 Oe. Such high M_S values with appreciable coercivity make it an ideal candidate for a soft phase.

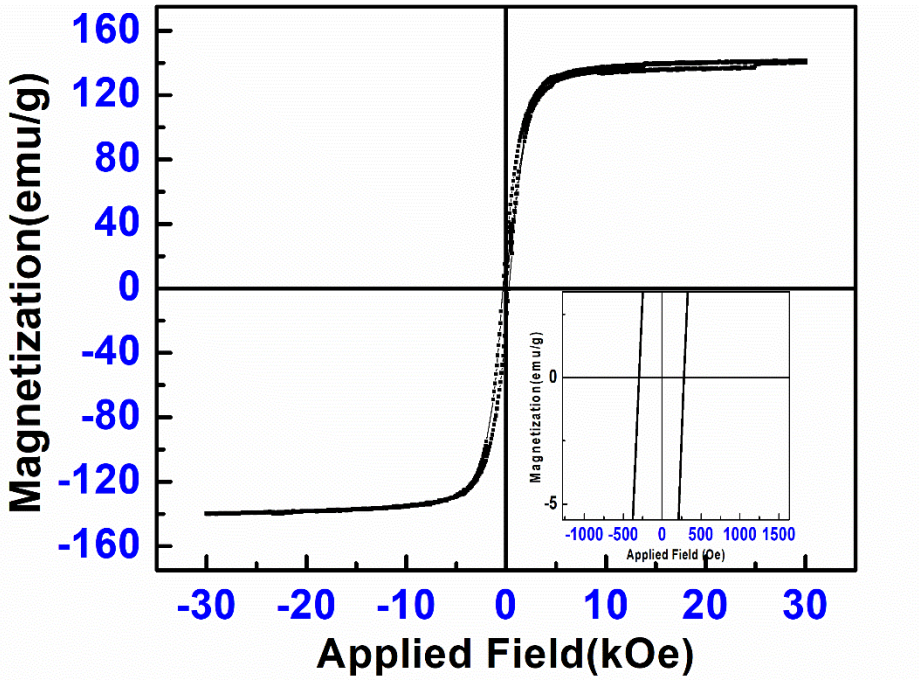

Figure 6.8. Room temperature M *vs*. H hysteresis plot of Co@C nanoparticles under ± 3 kOe**.** Inset shows the values extended near origin.

The obtained M_S and H_c values, which largely depend on the composition and particle size of the nanoparticle, are greater than that of earlier reports of Co@C [16]. The reported studies suggest that, temperature of synthesis also largely effects the Co@C magnetic properties [16]. The adoption of relatively higher temperature of 700 ºC for the preparation, enhance the crystallinity and particle size of the Co core resulting in the betterment of M_S value. The observed M_r/M_S ratio also suggests enhanced ferromagnetism of Co@C. In addition, the obtained M_S and H_C values are better than that of reported pure Co nanoparticles, which has a M_S of ~120 emu/g and a H_c of ~120 Oe[17]. The obtained greater values of H_C for the present sample can be attributed to the size effect. Further, the carbon layer weakens the dipole moment between Co nanoparticles and contributes in the improvement of coercivity. Literature also suggests that the anisotropy fields of fcc, hcp and fcc-hcp mixture

structured Co are around 0.46 T, 0.8T and 0.68 T respectively, assuring their decent coercivity values [18].

The Figure 6.9 shows the M vs H loops of the $(Mn_{55}Bi_{45})_{100-x}/(Co)_x$ (x=10,15, and 20 wt.%) nanocomposites. As discussed in prior chapters, the pure $Mn_{55}Bi_{45}$ alloy, after 2 h of cryo-milling, displayed a M_S value of 40.9 emu/g whereas its M_r and H_C values were around 20.9 emu/g and 6.7 kOe respectively. It can be observed that with the increasing content of the soft phase i.e. Co@C, the M_S values of the composites increased from 41 emu/g to 67 emu/g. Correspondingly, the M_r value also increased from 21 emu/g to 40 emu/g. The addition of a high anisotropy soft phase also resulted in a drastic improvement in coercivity values. Up to 15 wt%. of Co@C addition, a remarkable H_C value of 10.9 kOe was observed. Further additions, led to the decrease in the M_S , M_r and H_C values.

The enhancement in these magnetic properties suggests a strong exchange interaction between the soft and hard phases. It can be observed that greater percentages of (15%) soft phase could be incorporated in this nanocomposite without deterioration of magnetic properties. The prior utilized soft phases Fe_3C@C and FeNi@C were only limited to 10 and 15 wt.% respectively. Also, in comparison, the fall in coercivity values post highest percentage of addition of the soft phase, was also observed to be less drastic in the current nanocomposite. The variation in magnetic properties can be seen in the Figure 6.9b.

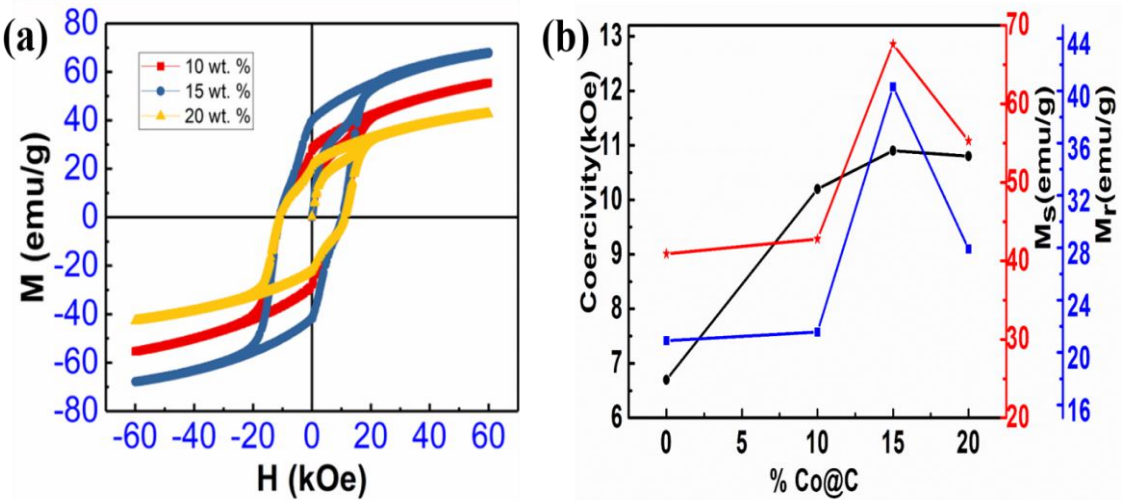

Figure 6.9. (a) M *vs.* H hysteresis plots under ± 6 kOe applied field at room temperature and (b) magnetic properties variation of $Mn_{55}Bi_{45}$/Co@C (10, 15 and 20 wt.%) nanocomposites after cryo-milling.

As discussed earlier, M_r/M_S ratio was found to be ~0.5 since the prepared nanocomposites are isotropic in nature. Better M_r/M_S ratio and consequently energy products can be obtained from the prepared nanocomposites by further compaction under external magnetic field [19]. The switching field distribution curves of the nanocomposites are in concurrence with the obtained magnetic properties. As shown in Figure 6.10, the SFD curves indicate the best exchange interaction for 15 wt.% sample, with a narrow single peak. The broad, double peaks of other nanocomposites are indicative of the poor exchange interaction between the hard-soft phases in them.

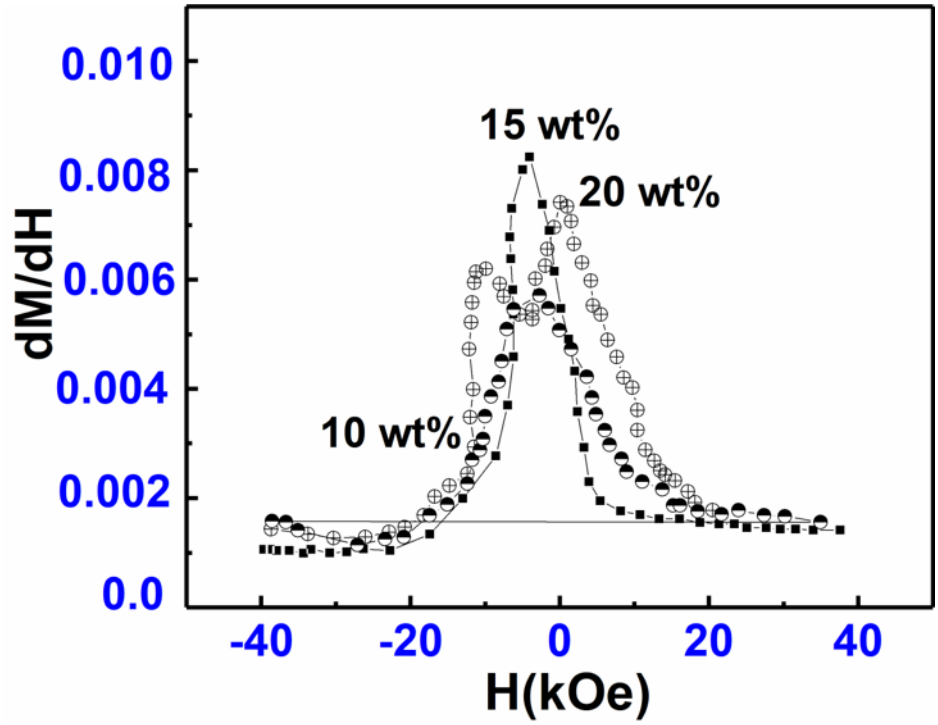

Figure 6.10. Switching field distribution curves of $(Mn_{55}Bi_{45})_{100-x}/(Co)_x$ (x=10,15, and 20 wt.%) nanocomposites.

Conclusions:

The Co@C nanoparticles with M_S~140 emu/g and H_C~470 Oe was synthesized and confirmed using XRD and TEM techniques. The nanoparticles consisted of two phases i.e., fcc Co and hcp Co. The carbon coating was continuous and connected as shown by TEM BF images. The Raman spectrum of the nanoparticles corroborated the presence of carbon. Among the $(Mn_{55}Bi_{45})_{100-x}/(Co)_x$ (x=10,15, and 20 wt.%) nanocomposites prepared by cryogenic milling, the 15 wt.% sample displayed optimum properties with H_C value of 10.9 kOe, M_S ~ 63 emu/g and M_r~38 emu/g. The nanocomposite exhibited better properties than the pure $Mn_{55}Bi_{45}$ cryomilled powders owing to the exchange coupling between the soft-Co

phase and hard-LTP. This also validates the usage of Co@C nanoparticles as the soft phase in exchange-spring magnets.

6.4. References

[1] Y.-K. Hong, J. Park, O.N. Mryasov, S.-G. Kim, S. Kim, J. Lee, G.S. Abo, C.-J. Choi, J. Lee, Magnetic properties of MnBi based alloys: First-principles calculations for MnBi-Co and MnBi-Co-Fe cases, AIP Adv. 3 (2013).

[2] Y.Q. Li, M. Yue, T. Wang, Q. Wu, D.T. Zhang, Y. Gao, Investigation of magnetic properties of MnBi/Co and MnBi/Fe65Co35 nanocomposite permanent magnets by micro-magnetic simulation, J. Magn. Magn. Mater. 393 (2015) 484–489.

[3] D.P. Dinega, M.G. Bawendi, A solution-phase chemical approach to a new crystal structure of cobalt, Angew. Chemie Int. Ed. 38 (1999) 1788–1791.

[4] O. Kitakami, H. Sato, Y. Shimada, F. Sato, M. Tanaka, Size effect on the crystal phase of cobalt fine particles, Phys. Rev. B. 56 (1997) 13849.

[5] A.S. Andreev, J.-B. d'Espinose de Lacaillerie, O.B. Lapina, A. Gerashenko, Thermal stability and hcp–fcc allotropic transformation in supported Co metal catalysts probed near operando by ferromagnetic NMR, Phys. Chem. Chem. Phys. 17 (2015) 14598–14604.

[6] Y. Lü, Y. Wang, H. Li, Y. Lin, Z. Jiang, Z. Xie, Q. Kuang, L. Zheng, MOF-derived porous Co/C nanocomposites with excellent electromagnetic wave absorption properties. ACS Appl Mater Interfaces 7 (24): 13604–13611, (2015).

[7] A.L. Patterson, The Scherrer formula for X-ray particle size determination, Phys.

Rev. 56 (1939) 978.

[8] N.L. Torad, M. Hu, S. Ishihara, H. Sukegawa, A.A. Belik, M. Imura, K. Ariga, Y. Sakka, Y. Yamauchi, Direct synthesis of MOF-derived nanoporous carbon with magnetic Co nanoparticles toward efficient water treatment, Small. 10 (2014) 2096–2107.

[9] Y.D. Zhang, J.I. Budnick, W.A. Hines, S.A. Majetich, E.M. Kirkpatrick, Microstructure and magnetic behavior of carbon-coated Co nanoparticles studied by nuclear magnetic resonance, Appl. Phys. Lett. 76 (2000) 94–96.

[10] J. Sui, C. Zhang, J. Li, Z. Yu, W. Cai, Microwave absorption and catalytic activity of carbon nanotubes decorated with cobalt nanoparticles, Mater. Lett. 75 (2012) 158–160.

[11] A.C. Ferrari, J. Robertson, Interpretation of Raman spectra of disordered and amorphous carbon, Phys. Rev. B. 61 (2000) 14095.

[12] F. Tuinstra, J.L. Koenig, Raman spectrum of graphite, J. Chem. Phys. 53 (1970) 1126–1130.

[13] R. Kumar, M. Manjunatha, A. V Anupama, K.P. Ramesh, B. Sahoo, Synthesis, composition and spin-dynamics of FCC and HCP phases of pyrolysis derived Co-nanoparticles embedded in amorphous carbon matrix, Ceram. Int. 45 (2019) 19879–19887.

[14] R. Clerac, F.A. Cotton, K.R. Dunbar, T. Lu, C.A. Murillo, X. Wang, New linear tricobalt complex of di (2-pyridyl) amide (dpa),[Co3 (dpa) 4 (CH3CN) 2][PF6] 2, Inorg. Chem. 39 (2000) 3065–3070.

[15] B.N. Papas, H.F. Schaefer, Homonuclear transition-metal trimers, J. Chem. Phys. 123 (2005).

[16] D.L. Leslie-Pelecky, R.D. Rieke, Magnetic properties of nanostructured materials, Chem. Mater. 8 (1996) 1770–1783. https://doi.org/10.1021/cm960077f.

[17] V.A. Bautin, A.G. Seferyan, M.S. Nesmeyanov, N.A. Usov, Magnetic properties of polycrystalline cobalt nanoparticles, AIP Adv. 7 (2017).

[18] M. Manjunatha, G.S. Reddy, K.J. Mallikarjunaiah, R. Damle, K.P. Ramesh, Determination of phase composition of cobalt nanoparticles using 59 Co internal field nuclear magnetic resonance, J. Supercond. Nov. Magn. 32 (2019) 3201–3209.

[19] N.V.R. Rao, A.M. Gabay, W.F. Li, G.C. Hadjipanayis, Nanostructured bulk MnBi magnets fabricated by hot compaction of cryomilled powders, J. Phys. D. Appl. Phys. 46 (2013) 265001.